Chapter 3

Imaging through turbid media

3.1 Introduction

Among the various applications of the study of wave propagation in random media like ocean optics[1], atmospheric optics[2], astrophysics[3], perhaps the most important one is that employed in biomedical optics[4]. The problem, termed "Imaging through turbid media" essentially aims at obtaining information of the size, shape and depth of a foreign object hidden inside a tissue. This object could be a malignant tumour or a bullet or a broken bone. The hazards of overusage of X-rays on human tissues are only too well-known, and the quest for an optical counterpart for these rays is a strong motivator for the study of imaging through turbid media using optical wavelengths.

The foremost and perhaps the only formidable difficulty in employing optical wavelengths for imaging is the scattering of light by tissues. Tissues and flesh and other such biomedical samples consist of fibrous organic materials which scatter light strongly. Hence, the presence of any foreign body inside such a sample cannot be detected because the original direction of propagation of light that exits the sample cannot be determined. More often than not, the term "imaging" implies obtaining shadowgrams of hidden objects, as obtained by X-rays. The study of light propagation through random media has helped in making breakthroughs in this field. From the various properties of scattered light like pathlength distribution, wave-vector distribution and others, it has now been possible to extract images of such foreign bodies that are otherwise invisible to the eye.

3.2 Ballistic, snake and diffuse photons

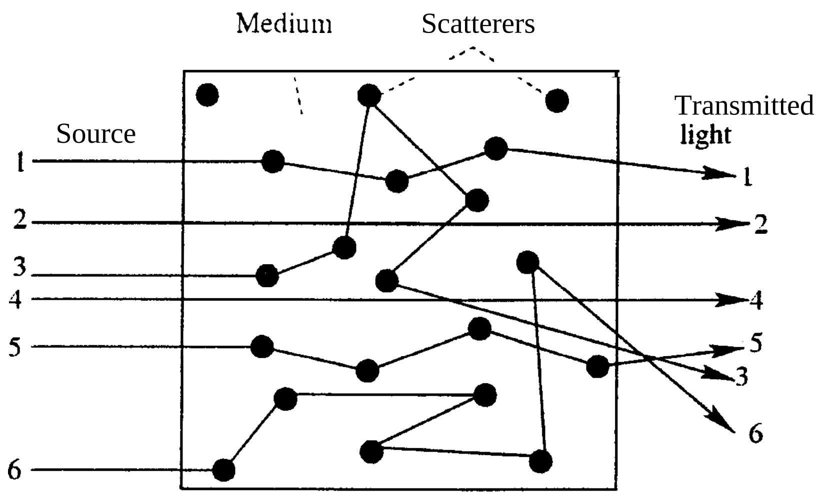

Figure 3.1: *A schematic illustrating the various kinds of photon paths inside the scattering medium. The shortest paths are the ballistic paths.*

Light inside a random medium can be regarded as consisting of three different parts[5], *viz.*, the ballistic or unscattered part, the diffuse or the multiply scattered part and the quasi-ballistic or weakly scattered part. The ballistic light travels unscattered and undeviated and is capable of forming a shadow of the opaque inclusion[1]. However, the multiply scattered diffuse light destroys this shadow due to its random direction. The role played by the quasiballistic light in these situations is most intriguing. The quasiballistic light is that which does undergo scattering, but only through small angles such that the deviation from the forward direction is small. These photons can be imagined to meander about the forward direction, like a snake. Indeed, such a picture used to describe quasiballistic light has led to its being called the "snake" light. We shall use the term snake light or snake photons extensively in this thesis. Figure 3.1 illustrates the above three types of

[1]It should be mentioned that imaging in the sense of shadowgraphy is possible only for opaque objects. For transparent and semitransparent objects, holographic techniques, which make use of the modulated phase of ballistic light, have been developed.

light inside the random medium. The figure shows six rays, labelled numerically, entering parallel to each other, as is the case when the source is collimated, like a laser. The various probable paths are shown inside, and the outgoing paths are tagged with their respective labels again. From the above description, we classify rays 2 and 4 as ballistic, 1 and 5 as snake and 3 and 6 as diffuse. Merely for simplicity, we have avoided showing two paths off the same scatterer, which is, by no means, disallowed. The role of each of these rays is illustrated in figure 3.2. The diffuse rays are responsible for washing out the

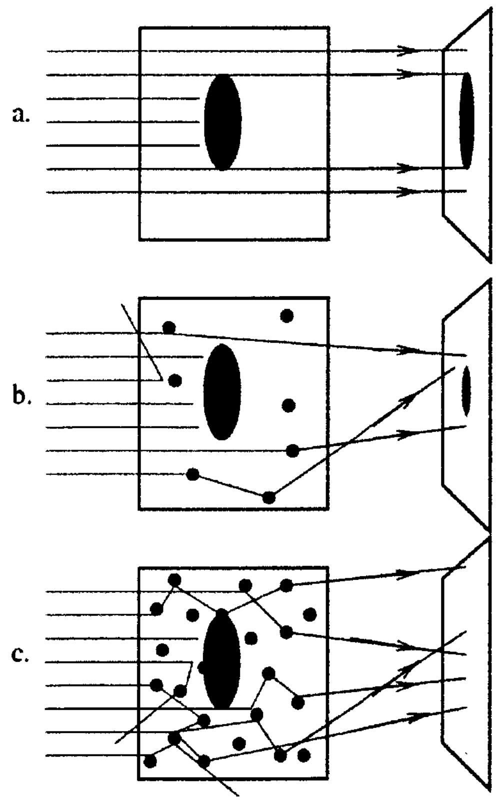

Figure **3.2:** *A schematic illustrating the effect of scattering on image formation. The clear shadow which is formed in the absence of a scattering medium (figure a) suffers from blurring of edges and reduction in image contrast upon addition of a few scatterers (figure b). This is the result of the weakly scattered light, or the snake light, described in the main text. In the presence of strong scattering (figure c), the shadow is completely washed out by the diffuse light.*

shadow completely. Though the snake light is responsible for blurring of the image, it is

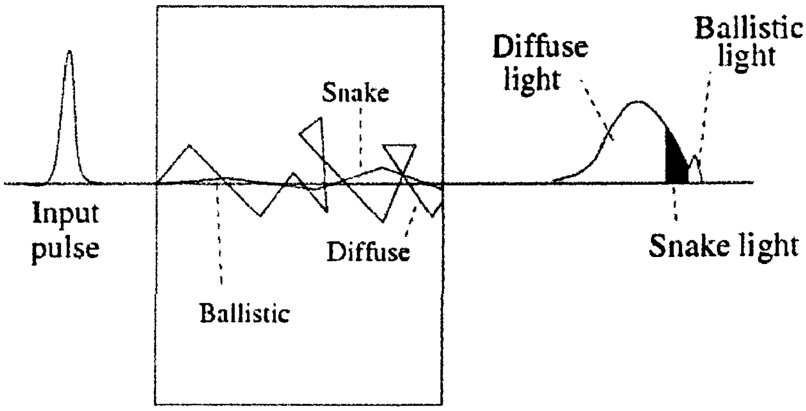

Figure 3.3: *Pulse broadening as a result of scattering. The output pulse is temporally separated into the ballistic, snake (shown in gmy) and the diffuse components.*

useful since it preserves its directional memory to some extent. Thus, in the methods of transillumination, it is important to separate the information carrying ballistic and the snake light from the diffuse noise. Indeed, all methods that have been developed, some of which are briefly introduced here, involve techniques to achieve the above separation, either spatially or temporally.

3.3 Time gating techniques of imaging

From figure 3.1, one physical characteristic of transmitted light that becomes immediately obvious as the possible "gate" to separate the ballistic and diffuse photons is the time of flight. As can be seen, the ballistic photons are the first to exit the medium, within a time equal to the thickness of the medium divided by the light velocity in the medium. Following the ballistic photons, the snake photons arrive slightly later, with a time distribution depending upon their pathlength distribution. Finally, the diffuse photons arrive last due to their tortuous paths inside the medium. The temporal distribution of the photons takes a shape shown in the figure 3.3. To the left of the scattering medium is shown the pulse of input light, that is stretched as it is transmitted through the wall. In the transmitted pulse, the small subpulse in the front corresponds to the ballistic photons, the leading part (shown in gray) of the main pulse is the snake part and the rest is the diffuse. One may employ a temporal gate that can shut fast enough, so as to admit the ballistic and snake part, and block the diffuse part. The intensity distribution of this filtered light directly shows the shadowgram of any object hidden inside the scattering wall. This method, called the temporal gating, has been, by far, the most used method for imaging through tissues, with more and more stress being laid upon finding shorter pulses and faster time gates. In a previously reported experiment, for an input pulse of 8 picoseconds, a time gate 20 picoseconds wide was employed, and submillimeter resolution was achieved[5]. Nowadays, femtosecond pulses are widely used for the purpose[6]. Time gating can be achieved by electronic means (Streak camera)[7], or using switches like Kerr shutter[8], or by employing nonlinear processes like second harmonic generation or Raman scattering[9]. The difference in pathlengths of the ballistic and diffuse photons also provides an alternative method of separating them[10]. A weakly absorbing material, when added to the random medium, absorbs the diffuse light more than the ballistic light, merely because the diffuse pathlengths are longer than the absorption length. The ballistic light is less probable to be absorbed because its pathlength is smaller than the absorption length. And in cases where the absorbing medium is a dye solution, one may change the concentration of the dye, and thereby the absorption length of the photons inside the medium. This method removes the diffuse noise by destroying it through absorption. This is an invasive method because of the need to add external absorbing agents.

Alternatively, a part of the input pulse can be made to overlap with the extended output pulse inside a Raman amplifier[11]. Since the amplifier is excited only for a short duration, only a part of the output pulse is amplified. The delay between the pump and the output pulse can be adjusted to amplify the ballistic part of the output pulse.

The above methods rely upon the extended paths of diffuse photons inside the random medium. These techniques necessarily require ultrashort pulses. There is another property of diffuse light that is exploited in imaging. As can be seen from the figure 3.1, the ballistic

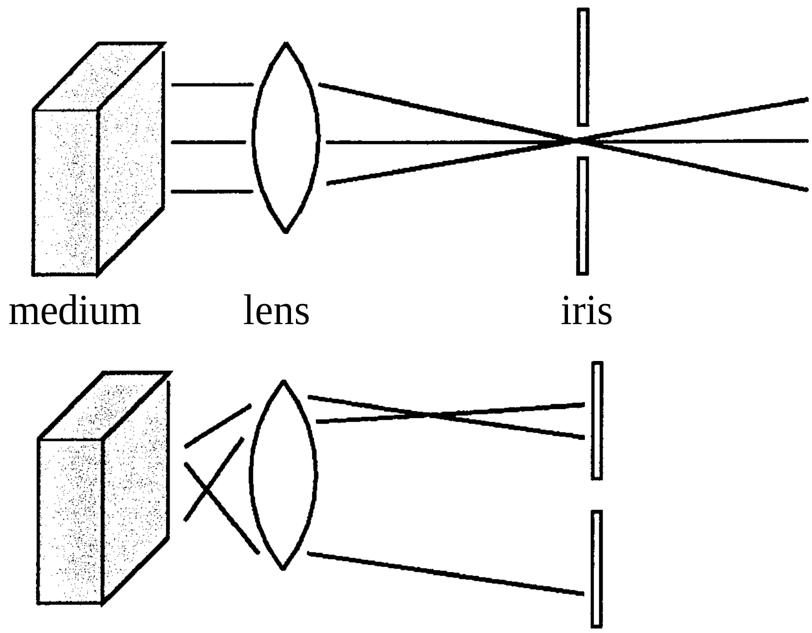

Figure **3.4:** *Spatial filtering : The light exiting in the forward and near-forward direction is focussed onto the aperture and let through, while that exiting at large deviation from the axis is blocked by the walls of the pinhole.*

light exits the medium undeviated from the original direction of propagation. The snake light, since is scattered only weakly, also exits at near forward directions. However, the multiply scattered diffuse light, that suffers scattering through large angles, exits the medium at large angles from the original direction of the input light. Hence, a lens placed after the scattering medium fourier transforms the transmitted intensity at the focal plane such that intensity at the lowest spatial frequencies[2] corresponds to the ballistic and snake light, and that at high spatial frequencies to the diffuse light.(Refer to Fig **3.4).** An iris placed at the focal plane allows only the ballistic and the snake light to pass through while blocking the diffuse. This is known as spatial filtering[12, 13]. However, this method is not capable of rejecting those diffuse photons that exit the medium at small angles. This noise results in low-contrast images.

Another method involving short times of ballistic light is fluorescence lifetime imaging[9].

[2]frequency, here, means the fourier conjugate variable of the angle

This method images imbedded inclusions that are fluorescent. The excitation is done by an ultrafast pulse, and the time required for the earliest arriving fluorescent photons is recorded. For ballistic excitation and ballistic fluorescent light, this time is equal to $\frac{2d}{v}$, where d is the distance of the object from the front surface and v is the speed of light in the medium. Using this technique, the authors could distinguish between two inclusions at different depths from the front surface, something that is out of capacity of shadow-graphic imaging. However, this method can be used only for fluorescent inclusions, which severely limits its applicability, and is also invasive, if fluorescent agents are externally added to the system. In contrast, the above time-of-flight methods are non-invasive and widely applicable.

3.4 Imaging using continuous-wave sources

If the ultrashort pulses are to be replaced by continuous wave light, an alternative to time-tagging has to be employed. Polarisation is one such alternative. The exact Mie theory of light scattering by small particles[14] calculates the mean angle of scattering, the transport mean free path and hence the time of flight of the photons inside the random medium. Apart from these, the theory also analyzes the effect of scattering on the polarisation of the input light. Depending upon the size and shape of the scatterer, a scattering matrix can be computed that connects the input and output polarisation vectors of the photon. Larger the angle of scattering, more is the depolarisation of linearly polarised light. Consequently, one expects that the depolarisation of a scattered photon can be an indicator of the path that the photon traverses in the random medium. Thus, along with the time-of-flight and the angle of exit of the photon, its polarisation can be used as an effective gate to separate the scattered photons from the unscattered ones.

Thus, it has been recognised that the initial state of polarisation is preserved for photons travelling along straight or nearly straight line trajectories while it is randomised for diffusing photons that have traversed the medium by a random walk. After a few experiments reported[15, 16, 17] that a temporal gate can be simulated by using this fact to separate the long path photons from the short path photons, Emile et al devised a scheme[18] to image through scattering media. In that experiment, light passing through a rotating linear polariser was made incident on a random medium. The emerging scattered light, after passing through a fixed analyzer, was collected by a detector by scanning across the exit face of the sample. Two pinholes, one before and another after the sample, permitted the image bearing photons to be detected. The resultant signal consisted of an oscillatory component due to the photons that still retained a significant amount of their original polarisation, riding on a constant background arising from the multiply scattered and completely depolarised light. Using lock-in detection to collect only the oscillatory component and a synchronised step scan of the entry and exit pinholes, it was possible to image millimeter sized objects immersed in milk.

We use a technique that does away with the pinholes and the scanning procedure[19]. This technique enables us to obtain two-dimensional images directly after grabbing the intensity distribution of the scattered light and analysing it for polarisation preservation. The details of this technique are described below along with the experimental setup that was used.

3.5 Experimental details

The figure 3.5 shows the schematic of the experimental setup used for imaging. An unpolarised orange HeNe laser (2.5 mW, 612 nm) was used as the continuous wave collimated source. The 2 mm wide beam of the laser was expanded to 8 mm using a beam expander. The expanded beam was passed through a polariser mounted on a stepper motor. The smallest angular step that the motor could rotate through was $\frac{360}{25000}^{\circ}$. By adjusting the number of impulses sent to the motor, it was possible to change the angular position of the polariser to the desired angle. The polarised beam emerging from the polariser was made incident on the sample holder. The sample holder used here was a glass cuvette of 10 mm

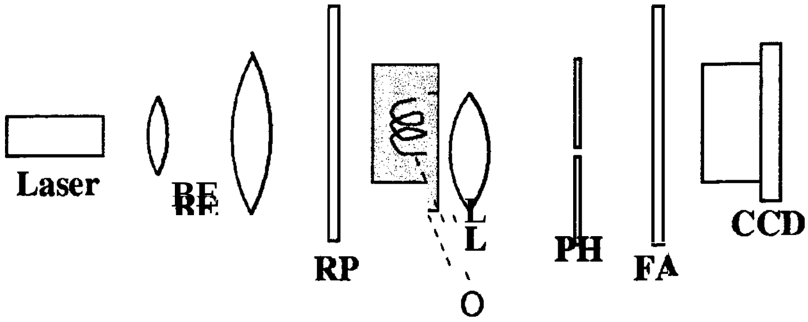

Figure **3.5:** *Setup used for imaging through turbid media using polarisation discrimination. BE : Beam Expander, RP : Rotating Polaroid, O : Object immersed in the scattering medium, L: Lens, PH : Pinhole, FA : Fixed analyser. The scheme of imaging is described in section **3.6.***

thickness. The sample used was a **1.67%** (by volume) colloidal suspension of **0.12** μ diameter polystyrene spheres in water. The scattering mean **free** path in this case turned out to be **298** μ and the transport mean free path, as calculated from the Mie theory, was **337** μ. The object immersed in the suspension was a small metallic helical spring. The total thickness of the medium was about **30** transport mean free paths. The spring could not be discerned with the naked eye even with intense incident light. **A** lens-pinhole system placed after the scattering sample carried out the spatial filtering by blocking the diffusive light emergent at large angles. The light admitted by the pinhole was passed through a fixed analyzer and made incident on an intensified CCD. The gain of the CCD was set at **2.** A sequence of frames was grabbed by the CCD, while the polariser was rotated through 10° between two successive frames. An individual frame was acquired for a time duration of **40** ms, and successive frames were separated by 1 s, when the polariser rotated to the next position. The intensity of the ouput light did not vary with the rotation of the polariser, implying that the diffuse component strongly overwhelms the ballistic component. **A** set of **240** frames was grabbed before the data were analyzed to extract the image.

3.6 Polarisation discrimination imaging

When the polariser rotated with a frequency w with time, the polarisation of the input light also rotated with the same frequency. At the focal plane of the lens, where the pinhole was placed, the scattered light was spatially filtered and the light that was transmitted through the pinhole consisted of the ballistic, the snake and a reduced diffusive component. The ballistic light had the plane of polarisation rotating with the frequency w, and as it passed through the fixed analyser, its intensity exhibited a $\cos^2 wt$ variation with time. Any diffuse light that sneaked through into the signal had a randomised polarisation, and did not show any variation in intensity with time.

The raw data for imaging consisted of a sequence of **frames** (usually taken as 240 in our experiments) ordered in time. The frame grabber converted the light intensity falling onto the CCD into a **two-dimensional** matrix of size 512 x 512, with a one-to-one corespondence between the intensity falling on the $(i,j)^{th}$ pixel and the $(i,j)^{th}$ value of the matrix. A time series for each $(i,j)^{th}$ pixel was constructed by arranging the 240 values of the pixel in a vector in the order as they were collected. This timeseries was fourier transformed by using a one-dimensional FFT subroutine.

It is obvious that the pixels that fall within the geometric shadow of the object could not receive the ballistic photons as these were blocked by the shadow. They received only the near-forward and the diffuse light. The pixels outside the shadow received the ballistic light along with the diffuse light. So, when a time series was fourier transformed, then it showed a single peak at the zero frequency if the pixel received light of a constant intensity. Such a pixel had to be within the shadow. If, on the other hand, the fourier transform showed three peaks, one at the zero frequency and two identical peaks symmetrically placed about the central one, it implied that the intensity falling on that pixel was modulated, and the modulation was (the inverse fourier transform of the above three-peaked function) a cosine modulation. This just corresponded to the $\cos^2 wt$ modulation of the ballistic intensity, the peaks of the FFT being at +2w and -2ω. The amplitude of the FFT at the frequency 2ω was directly proportional to the ballistic intensity falling on it. So, we constructed a 512×512 matrix in which, the $(i,j)^{th}$ element was the amplitude of the peak at frequency 2ω in the respective fourier transform. Thus, we reconstructed the image, pixel by pixel. A matrix made of the zero frequency amplitudes was also constructed, for the sake of comparison. The zero frequency here corresponded to the total intensity falling onto the pixel till the data collection was in process.

Figure 3.6 shows the zero frequency matrix, where one can see hexagonal shaped cells. These are present on the protective plate covering the CCD sensitive element. Figure 3.7 shows the image at the frequency 2ω. The efficiency of this method of imaging is obvious. On close inspection of the reconstructed image, it is just possible to resolve the diffraction lines around the shadow of the object. When the real shadow of the object was imaged in the absence of the scattering medium, this diffraction lines were found to be less than one millimeter thick. From these observations, and from other imaging experiments, we could infer that the resolution of this imaging technique is around 100μ.

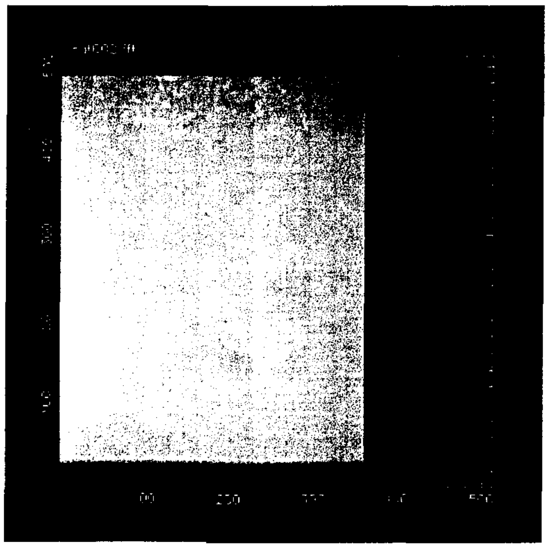

Figure 3.6: *Image reconstructed by using the zero frequency amplitude values of the fourier transform of the timeseries of modulated intensity. The image is an indicator of the total intensity falling onto the CCD.*

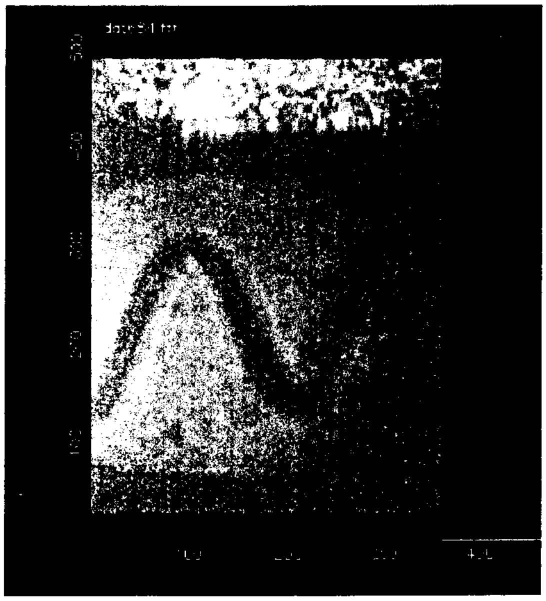

Figure **3.7:** *Image reconstructed using the amplitude at the correct frequency. Correct frequency is twice the frequency at which the rotating polariser is rotated. The image of the helical spring is obvious, and traces of diffraction lines around the shadow are noticeable.*

3.7 Stereographic imaging through turbid media

As mentioned earlier, the methods of transillumination suffer from one disadvantage, and that is the loss of the depth information of the object. For example, if one inserted two pins inside the random medium, such that one was ahead of the other and also laterally separated, the shadowgram would just show two pins, suppressing the depth information. From the figure **3.7,** it is impossible to ascertain whether the object is a flat S-shaped object or a spiral. Indeed, this information could be of prime importance in cases of malignant tumours where it is necessary to know even the longitudinal spread of the tumour. For such applications, it is required to devise a three-dimensional imaging technique.

We find a way out of this difficulty by constructing' three-dimensional images using stereography. Stereography makes use of the way in which the eyes see a three-dimensional object. For a person with normal binocular vision, each eye sees an object from a slightly different perspective. The two views are reconstructed by the brain to get a **3D** view of the object. Thus, if each eye is forced to see a different perspective of the same picture, the brain tries to fuse the two images to produce a perception of depth.

The way we exploited this fact was as follows. In the experimental setup, the cuvette containing the sample and the object was kept on a rotating table, that could rotate about the vertical axis through the centre of the cuvette. Care had to be taken to ensure that this vertical axis also passed through the centre of the object. This was achieved by first pasting the spring to the bottom of the cuvette in the centre and then adding the scattering medium. Data were then collected as described earlier. Then the rotating table was rotated through 10°, and data were collected again. Thus we obtained two sets of data, each one corresponding to an image that was in a slightly different perspective from the other. The images were extracted by analyzing the data as mentioned earlier. The two images were then pasted side to side at a convenient separation, making a stereogram shown in figure **3.8.** On viewing the stereogram, one can make out the approximate longitudinal extent of the object.

Figure **3.8:** *Stereogram of the spring. Three dimensional view is obtained by viewing the left image by the left eye and the right image by the right eye.*

The way to see the 3D image is as follows. Hold the paper at a convenient distance at the level of the nose. Slowly relax your eyes, so that they focus at a point behind the paper. You will the sense each image split into two, thus "seeing" four different images. Change the point at which the eyes have focussed, such that the two images in the middle slowly merge. At this point, the image that is seen by the brain shows 3D character. The stereogram of the spring is attached underneath. The two images here were negated to achieve ease of viewing.The stereogram shows that the upper and the lower arm of the spring are closer to the observer than the central arm, implying that they were towards the CCD camera when the object was being imaged. Thus, by this method of stereography, we can infer about the depth of multiple objects, or different parts of the same object.

Thus, we have devised a simple method to form three dimensional images of objects in turbid media. Instead of using expensive ultrashort pulses, inexpensive, low power continuous wave lasers (He-Ne or diode lasers) can be used. The setup is compact and portable, and images can be obtained within minutes.

Bibliography

[1] **V.** L. Granatstein, M. Rhinewine and A. M. Levine, Appl. Opt. **11, 1870 (1972).**

[2] **J.** S. Ryan and A. I. Carswell, J. Opt. Soc. Am. 68, **900 (1978).**

[3] S. Chandrasekhar, Radiative transfer, (Clarendon Press, Oxford, **1961).**

[4] Time resolved imaging and diagnostics in medicine, J. G. Fujimoto ed., Optics and Photonics News, October **1993.**

[5] L. Wang, P. P. Ho, C. Liu, G. Zhang, R. R. Alfano, Science, 253, **769 (1991).**

[6] Feng Liu, K. M. Yoo and R. R. Alfano, App. Opt. 32, **554 (1993).**

[7] **J.** C. Hebden, R. A. Kruger and K. S. Wong, App. Opt. 30, **788 (1991).**

[8] L. M. Wang, P. P. Ho and R. R. Alfano, App. Opt. 32, **535 (1993).**

[9] **J.** Wu, Y. Wang, L. Perelman, I. Itzkan, R. R. Dasari and M. Feld, App. Opt. 34, **3425 (1995).**

[10] **K. M.** Yoo, Feng Liu and R. R. Alfano, Opt. Lett. 16, **1068 (1991).**

[11] **M.** D. Duncan, R. Mahon, L. L. Tankersley and J. Reintjes, Opt. Lett. 16, **1868 (1991).**

[12] M. Shih and E. Leith, App. Opt. 34, **1310 (1995).**

[13] **Q. Z.** Wang, X. Liang, L. Wang, P. P. Ho and R. R. Alfano, Opt. Lett. 20, **1498 (1995).**

[14] G. Mie, Ann.Physik, 25, **337 (1908).**

[15] J. M. Schmitt, A. H. Gandjbakhche and R. F. Bonner, Appl. Opt. 31, 6535 (1992).

[16] Stephen P.Morgan, Man P.Khong and Michael G. Somekh, Appl. Opt. 36, 1560 (1997).

[17] X. Liang, L. Wang, P. P. Ho and R. R. Alfano, Appl. Opt. 36, 2984 (1997).

[18] O. Emile, F. Bretenaker and A. Le Floch, Opt. Lett. 21, 1706 (1996).

[19] H. Ramachandran and A. Narayanan, Opt. Commun. 154, 255 (1998).

Chapter 4

The Coherent backscattering effect

4.1 Introduction

Under the diffusion approximation, one assumes that the wave propagation is diffusive in character after multiple scattering. However, the diffusion equation predicts a smooth spatial variation for intensity transmitted through a slab of scatterers. Contrary to that, the transmitted light, and also the back-scattered light, consists of random bright and dark spots which form the so-called speckle pattern that results from the interference of the various scattered waves. Upon averaging the various speckle patterns by changing the configuration of the scatterers, smooth transmitted intensity profile can be obtained in agreement to the diffusion theory. In samples like aqueous suspensions of polyballs, the Brownian motion of the polyballs automatically carries out the configurational averaging, and a smooth intensity is seen when the detector is not fast enough to grab the flickering speckle patterns. Yet, another interference effect exists in a multiply scattering medium that manifests itself inspite of averaging the speckle pattern. This effect is observed only in the backscatter direction, and is known as the coherent hackscattering effect[1, 2]. It originates from the interference of light waves travelling in the backscattering direction. This dramatic effect has been studied extensively through a series of experiments and theoretical analyses[1-7].

We can understand the origin of the coherent backscattering (CBS) effect from fig-

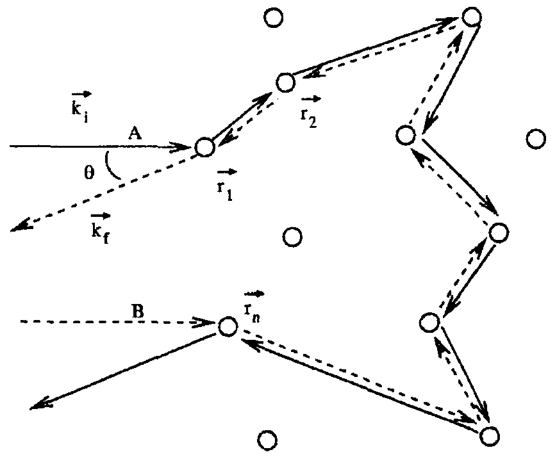

Figure 4.1: *A schematic showing two time-reversed light paths inside a random medium, giving rise to intereference in the backscatter direction.*

ure 4.1 that depicts some light trajectories in a medium consisting of randomly placed static scatterers. The ray **A,** having a complex amplitude A_i at some far away source point $\mathbf{R}_0$, enters the medium with a wave-vector $\mathbf{k_i}$, and exits from the front surface with the wave-vector $\mathbf{k_f}$. Before exiting, it undergoes multiple scattering off the random centres placed at $\mathbf{r_1}$, $\mathbf{r_2}$ .....$\mathbf{r_n}$. The ray **A** has a complex amplitude A_0 at some far-away observation point $\mathbf{r_0}$. The ray B, enters the medium with the wave-vector $\mathbf{k_i}$, and also experiences n scatterings off the same scattering centres as above, *but in the reverse order.* Namely, the path B, ehaving a complex amplitude B_i (which is equal to A_i because they originate from the same source) at the source point $\mathbf{R}_0$, starts at the position $\mathbf{r_n}$, scatters off the sites $\mathbf{r_n}$,$\mathbf{r_{n-1}}$,...$\mathbf{r_2}$, $\mathbf{r_1}$, and ends at $\mathbf{r_1}$, and exits the medium with the wave-vector $\mathbf{k_f}$. **B** has the complex amplitude B_0 at the observation point $\mathbf{r_0}$. In other words, the ray path **B** can be regarded as the ray path **A** propagating backward in time between $\mathbf{r_1}$ and $\mathbf{r_n}$.

The amplitudes A_0 and B_0 at the point $\mathbf{r_0}$ can be related to A_i and B_i as

$$
\begin{aligned}
A_0 &= A_i\, exp[i\mathbf{k_i} \,.\, (\mathbf{r_1} - \mathbf{R_0}) + i\mathbf{k_{1,2}} \,.\, (\mathbf{r_2} - \mathbf{r_1}) + ... \\
&\quad + i\mathbf{k_{n-1,n}} \cdot (\mathbf{r_n} - \mathbf{r_{n-1}}) + i\mathbf{k_f} \cdot (\mathbf{r_0} - \mathbf{r_n})]
\end{aligned} \tag{4.1}
$$

$$
\begin{aligned}
B_0 &= B_i\, exp[i\mathbf{k_i} \cdot (\mathbf{r_n} - \mathbf{R_0}) + i\mathbf{k_{n,n-1}} \cdot (\mathbf{r_{n-1}} - \mathbf{r_n}) + ... \\
&\quad + i\mathbf{k_{2,1}} \cdot (\mathbf{r_1} - \mathbf{r_2}) + i\mathbf{k_f} \cdot (\mathbf{r_0} - \mathbf{r_1})]
\end{aligned} \tag{4.2}
$$

Here, $\mathbf{k_{n-1,n}}$ is the wave-vector of the ray propagating from the scatterer n − 1 to n. In the above expressions, we have dropped a factor that accounts for the scattering strength and any other effects due to the scatterer, since the scatterers are the same in the two paths.

Since $A_i = B_i$, we have

$$
\frac{A_0}{B_0} = exp\,[i(\mathbf{k_i} + \mathbf{k_f})\,.\,(\mathbf{r_1} - \mathbf{r_n})] \tag{4.3}
$$

Thus, $A_0 = B_0$ when $\mathbf{k_i} = -\mathbf{k_f}$, **i.e**, in the exact backscatter direction.

The same is obvious from the phase difference between the two paths. B_0 has an extra phase $-\mathbf{k_i} \cdot (\mathbf{r_1} - \mathbf{r_n})$ because the path B is longer at incidence, whereas A_0 has an extra phase $\mathbf{k_f} \cdot (\mathbf{r_1} - \mathbf{r_n})$ because the path A is longer at exit. Thus, in the case when $\mathbf{k_i} = -\mathbf{k_f}$, the two cancel, and the two outgoing rays are exactly coherent in the direction opppsite to the incident direction. The coherence drops as one deviates from the back-scattering direction.

Although here we discussed only two time-reversed light paths, there exist an infinite number of light paths within the random medium. For each such path, there always exists a time-reversed path which has exactly the reverse order of scattering. The final amplitude at the point of observation is then the sum total of all such pairs of time-reversed paths.

However, the interference maximum in the backscatter direction occurs only when the system is invariant under time-reversal. For instance, if the scatterers have velocities large enough that the time-reversed paths do not see the same position of scatterers, the above theory is inapplicable. While, in the case of light scattering, the wave speed is too high to be affected by moving scatterers, in electronic systems the moving scatterers may play a significant role.

From the above discussion, we can see that the intensity in the exact backward direction is larger than the intensity in other backscatter directions. Reverting to the picture of two counter-propagating waves, this intensity at the observation point due to A and B is given by

$$
\begin{aligned}
|A_0 + B_0|^2 &= |A_0|^2 + |B_0|^2 + A_0 B_0^* + A_0^* B_0 && (4.4)\\
&= |A_0|^2 \; |1 + exp[-i(\mathbf{k_i} + \mathbf{k_f}).(\mathbf{r_1} - \mathbf{r_n})]|^2 && (4.5)\\
&= 2\{1 + cos[(\mathbf{k_i} + \mathbf{k_f}).(\mathbf{r_1} - \mathbf{r_n})]\} \; |A_0|^2 && (4.6)
\end{aligned}
$$

where we have used the equation 4.3, to express B_0 in terms of A_0.

Inside the curly brackets, the constant 1 is just the sum of the individual intensities of the two rays $|A_0|^2 + |B_0|^2$, i.e., the incoherent scattered intensity. The cosine term, $cos[(\mathbf{k_i} + \mathbf{k_f}) . (\mathbf{r_1} - \mathbf{r_n})]$ is due to the interference term $A_0 B_0^* + A_0^* B_0$. Thus, in absence of any interference effects, the incoherent scattering would simply be $2A_0$. As we saw earlier, the intensity due to interference would be maximum in the exact backscatter direction, i.e., when $\mathbf{k_i} = -\mathbf{k_f}$. In that case, we see that the argument of the cosine term goes to zero in the equation 4.6, and the intensity adds up to $4A_0$. Thus, the intensity in the backscatter direction is enhanced by a factor of 2. This is the so-called enhancement factor in coherent backscattering. One may obtain an order of magnitude estimate for the angular width of the CBS cone from the above phase difference. Let $|\mathbf{r_1} - \mathbf{r_n}| = $ R, and 0 be the scattering angle as shown in the figure 4.1. Let α be the angle between $(\mathbf{k_i} + \mathbf{k_f})$ and $(\mathbf{r_1} - \mathbf{r_n})$. Then, writing $|(\mathbf{k_i} + \mathbf{k_f})|$ as $2sin(\theta/2)$, we get the phase difference $\Delta\phi$ as

$$
\begin{aligned}
\Delta\phi &= \frac{2\pi}{\lambda} 2sin(\theta/2) R cos\alpha \\
&= \frac{2\pi}{\lambda}\theta R && (4.7)
\end{aligned}
$$

for small 0 as is the case in experimentally realised situations, where 0 is of the order of milliradians. Here we assumed α to be zero, since, for a strong scattering sample, $(\mathbf{r_1} - \mathbf{r_n})$ will be nearly parallel to the sample surface, and so will $(\mathbf{k_i} + \mathbf{k_f})$, for angles away from the exact backscatter. The mean-squared separation between the first and the last scatterer in the diffusion approximation is given as $< \mathrm{R}^2 >= 6(\frac{cl^*}{3})t$ where t is total path time, and c is the light velocity in the medium. Taking the rms value for R, we get,

$$\Delta\phi = \frac{2\pi}{\lambda}\theta\sqrt{2l^*s} \tag{4.8}$$

where $s = ct$, the total pathlength inside the medium. For constructive interference to occur, the phase difference $\Delta\phi \ll 2\pi$. This will happen below a certain angle θ given by

$$\theta = \frac{\lambda}{\sqrt{2l^*s}} \tag{4.9}$$

The maximum angular width that the cone can attain is when s is smallest, which can be, at the minimum, equal to the transport mean free path l^*. Thus

$$\theta = \frac{\lambda}{\sqrt{2}l^*} \tag{4.10}$$

However, this is only an approximate expression, and the exact theory for isotropic scatterers predicts the width of the cone to be given by[5, 6]

$$W \simeq \frac{0.7}{2\pi}\frac{\lambda}{l^*} \tag{4.11}$$

Thus, the conewidth varies in inverse proportion with l^*. The diffusion approximation has been applied to obtain an analytic expression for the lineshape of the coherent backscattering cone. This lineshape is given by[7]

$$I(q) = \frac{1}{2}\frac{3}{8\pi}\left[1 + 2\frac{z_0}{l^*} + \frac{1}{(1+ql^*)^2}\left(1 + \frac{1-e^{-2qz_0}}{ql^*}\right)\right] \tag{4.12}$$

4.2 Experimental details

The experimental setup that was used for studying coherent backscattered light is shown in the figure 4.2. A He-Ne laser ($\lambda = 0.612\mu$, 2.5 mW) was used as the continuous wave source. The beam of width 2mm was expanded using a beam expander to a width of 6mm and then passed through a polariser to make its polarisation vertical. The polarised beam was split by a non-polarising beamsplitter, which reflected part of the beam onto the sample, while the transmitted beam was dumped into a beam dump. As shown in the

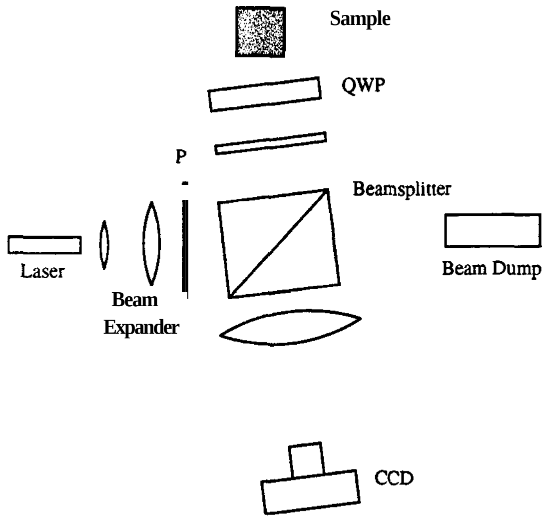

Figure 4.2: *Experimental setup for studying the coherent backscattering from random media. The Michelson Interferometer configuration has its two arms non-orthogonal to each other to avoid multiple reflections interfering with the weak back-scattered signal.*

figure 4.2, although a Michelson interferometer was used for the detection of backscatter, the angle between the two arms of the interferometer configuration was slightly off 90°. This was done to avoid multiple reflections between the faces of the cube beamsplitter. The sample used was an aqueous suspension of spherical PMMA (Polymethyl metha-acrylate, refractive index n = 1.495, diameter 0.195μ) microparticles contained in a cuvette of width lcm. The cuvette was placed such that the beam was incident upon the front face at a non-normal incidence, to prevent the specular reflection off the front face from interfering with the signal. An analyser was placed after the beamsplitter with its polarisation axis parallel to the vertical. This was followed by a quarter wave plate, that was placed with its slow axis making an angle of 45" with the vertical. Thus, the light incident upon the sample was circularly polarised. Light that was scattered off inhomogeneities on the cuvette face, and also that was singly scattered from the sample, flipped its helicity and was converted to linearly polarised light during the second pass through the quarter wave plate, with the plane of polarisation orthogonal to the analyser axis. This was then blocked by the analyser and only the multiply scattered light was let through. This light was focussed by a lens of focal length 30cm onto a CCD camera . The CCD was kept at the focal plane of the lens, so that the angle of backscatter 8 and the linear extent d of the CBS curve on the CCD were fourier conjugate variables, related by the expression d = f sin8 = $f\theta$, for small 8. A frame grabber grabbed the intensity distribution falling onto the CCD camera at the rate of one frame per two seconds. A total of twenty frames were grabbed, during which the cuvette was vibrated so that stray reflections were averaged out, while the CBS signal was enhanced. The image was then analysed to obtain the cross-section through the diameter of the CBS spot which was the CBS curve. Two different CBS curves were obtained, one for a volume fraction of 0.1, and the other for a volume fraction of 0.05 of the scatterers.

4.3 The coherent backscattering cone

Figure 4.3 shows the CBS curve obtained in the case of the sample with a volume fraction of 0.1. The curve looks unsymmetrical with the right wing slightly lower than the left wing. This is because of slight misalignment in the focussing of the backscattered beam on the CCD. However, the difference between the two wings is quite small and does not affect the results. Using the noise value in the left wing, the enhancement factor turns out to be 1.79, while using that in the left wing, it comes out to be 1.92.

From theoretical calculations based on the Mie theory for small particles[8, 9], the $< cos\theta >$ of the above particles, where 8 is the angle of scattering, turns out to be 0.312. Hence the transport mean free path for the above 10% suspension turns out to be 59μ. From equation 4.11, we estimate the cone angle to be 1.2 millirad, while from the experimental curve, the width at the half maximum is seen to be 1.5 millirads, in excellent agreement with the theory.

Figure 4.4 shows the same CBS curve along with the curve predicted by the diffusion theory, i.e., equation 4.12. The theoretical curve was plotted with a transport mean free path obtained by performing a least squares fit on the experimental curve. The best fit

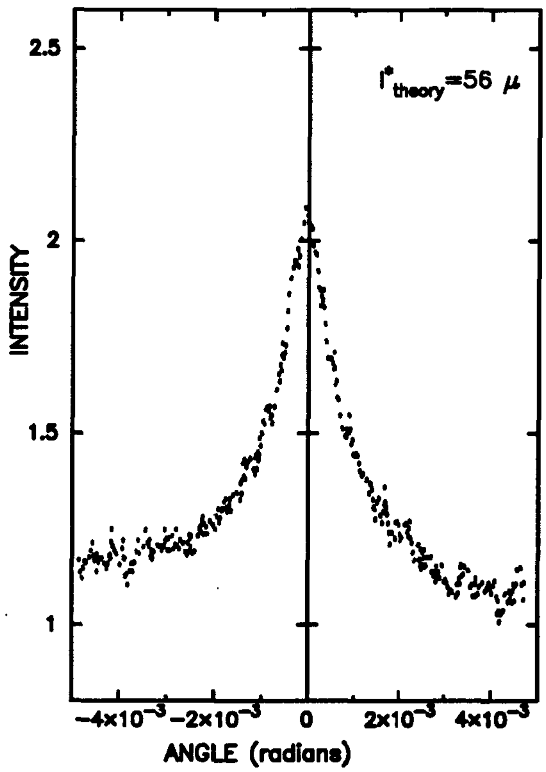

Figure **4.3:** *Backscattered intensity plotted as a function of angle, from a sample of* $l^* = 56\ \mu$.

code was based on the Marquardt-Levenberg algorithm for nonlinear fits, for a single parameter. We give underneath only a skeleton of the algorithm. For a detailed explanation, the reader may refer to any book on numerical recipes, for example, reference [10].

The algorithm uses an iterative scheme to reduce the squared difference between the experimental curve and the theoretically predicted curve to a value lower than the acceptable error, and has the advantage of rapid convergence. Following are the steps of the algorithm:

1. Make an initial guess for l^*, say a which will best fit the function $y(x)$ to the data with the number of datapoints N.

2. Find $\chi^2(a)$,

$$\chi^2(a) \quad = \quad \sum_{i=1}^{N}\left[\frac{y_i - y(x_i;a)}{\sigma_i}\right]^2$$

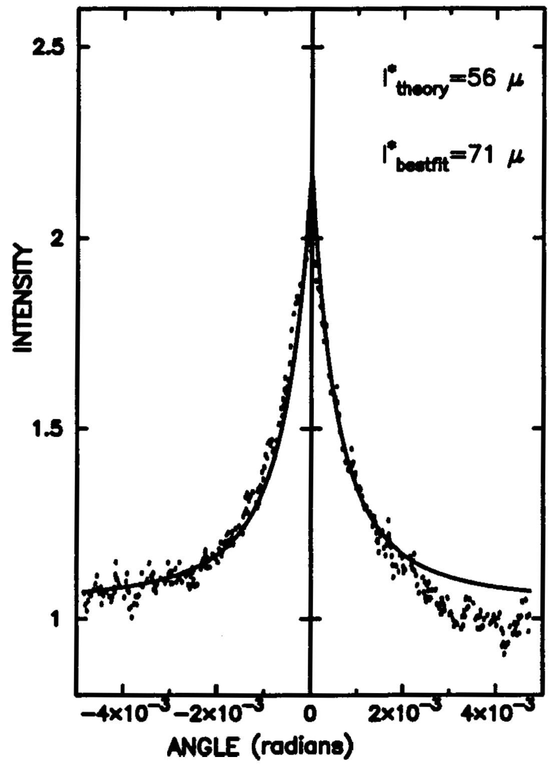

Figure **4.4:** *The least squares fit using the equation 4.12 to the data of figure 4.3* where y_i = i^{th} data value, and

$y(x_i;\text{a})$ = value calculated from the nonlinear function, at point xi, using the value a for l^*.

σ_i = measurement error in the i^{th} datapoint. If unknown, $\sigma_i = 1$, for $\forall i$.

3. Choose a constant λ, say $\lambda = 0.001$.

4. Solve the following equation for δa.

$$\begin{aligned}
\alpha(1+\lambda)\delta a &= \beta \\
\textbf{where } \beta &= \sum_{i=1}^{N}[y_i - y(x_i;a)]\frac{\partial y(x_i;a)}{\partial a} \\
\textbf{and } \alpha &= \sum_{i=1}^{N}\left[\left(\frac{\partial y(x_i;a)}{\partial a}\right)^2 - [y_i - y(x_i;a)]\frac{\partial^2 y(x_i;a)}{\partial a^2}\right]
\end{aligned}$$

5. If $\chi^2(\text{a}+\delta a) \geq \chi^2(\text{a})$, increase λ by 10 and go to step 4. If $\chi^2(\text{a}+\delta a) < \chi^2(\text{a})$, decrease λ by 10 and go to step 4.

6. STOP, when $|\chi^2(a+\text{ba}) - \chi^2(\text{a})| <$ E, where one may choose ϵ to be a small value like 0.1.

The value a, then, is the bestfit value for the parameter l^*.

Using the above algorithm for fitting the data with the curve predicted by the diffusion approximation, we obtained a value for l^* equal to 71μ. while the Mie theory gives a value 59μ. Recalling the asymmetry in recording the data due to an experimental artefact, the CBS curve was made symmetrical by force, by susbtituting the right wing by the image of the left wing. Upon fitting this "symmetrised" curve, we obtained the value of I* equal to 64μ. The data and the least squares fit is illustrated in figure 4.5.

As discussed earlier, the cone width varies inversely as the transport mean free path. To verify this, a CBS curve was obtained from a sample of the same rnicrospheres, this time the volume fraction being 0.05. Thus the transport mean free path was doubled to 112μ. Figure 4.6 shows the experimentally obtained CBS curve along with the curve predicted by the diffusion theory. The bestfit value for I*, here, was 146μ. The cone width obtained from equation 4.11 is equal to 0.6 milliradians, and the width at the half maximum of the experimental curve is equal to 0.9 milliradians. Thus, we obtained excellent agreements

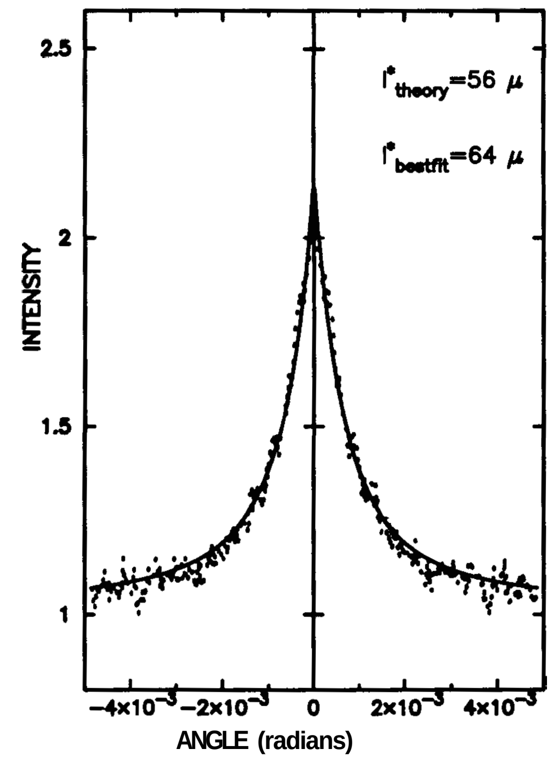

Figure 4.5: *Least squares fit, after making the cone symmetric by substituting the right wing of the cone by the image of the left wing.*

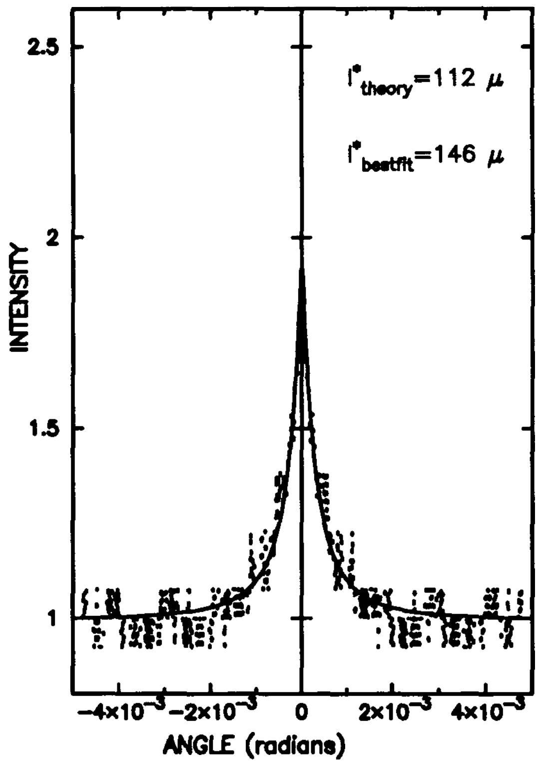

Figure 4.6: CBS *data and its least squares fit for a sample of* $l^* = 112\mu$. *The halving of the CBS cone angle on doubling of* l^* *is obvious on comparison with figure 4.5*

between the theory and our CBS curves for different scatterer strengths. We tabulate our results as follows.

Also known as "weak localisation", the phenomenon of enhanced backscattering is a precursor to the regime of strong localisation. A sufficient increase in the strength of disorder results in permanent trapping of photons inside the random medium. Yet, it is a formidable task to increase the strength of disorder so that it just crosses the critical disorder required to localise photons. Special materials are required to achieve this disorder[11]. In contrast, the phenomenon of CBS is observed with more common substances like polyballs suspended in water and is easier to observe experimentally, provided the delicate alignment and noise filtering is taken care of.

Set no.	Enhancement factor	θ_{theo}	$\theta_{best fit}$	l^*_{theo}	$l^*_{best fit}$	χ^2
1	1.785	1.2	1.5	56	71	0.0001342
2	1.74	0.6	0.9	112	146	0.000324

Table 4.1: *Comparison of CBS parameters obtained theoretically and experimentally.*

4.4 Enhancement of signal over noise

However, there is a drawback to this exciting experiment in that the CBS cones from weak scattering samples are extremely weak. The coherent signal that has to be demarked from the incoherent noise is too obscure, and usually difficult to separate out. The theoretically predicted enhancement of 2 is approachable only in strong scattering samples, like the one used above in our experimental studies. The weak samples not only backscatter less, but also narrow the cone such that it is rendered smaller than one pixel of the CCD. This problem is easily solved, though, by either using a photomultiplier or a lens of different focal length. Still, the problem of the signal being too weak and overwhelmed by the noise persists.

The noise affecting the CBS signal has several contributions, *viz* the incoherent backscattered noise, the CCD dark current, the scatter from the surrounding equipment (which results into a speckle pattern) and stray light in the room which usually is the result of diffuse light from leaks in the walls. The incoherent backscattered noise is the "desirable" noise, since it forms the background to the CBS signal. The CCD dark current and the stray light can be corrected by measuring the CCD signal when the laser light is off. We have devised an alternative method of measuring this noise as follows, and can be used when a colour CCD camera is employed. In such a camera, the light falling onto a pixel is measured as a set consisting of three values, the red, green and blue fraction of the incident light. Since the laser used in the experiment is either orange or deep red, the green and blue values are measures of the stray light and the CCD noise. The average of the green and blue values is a reasonable index of the above noise. This method, however, has to be cautiously used, because high intensity levels of the incident light can generate spurious values of the green and blue matrices. The scatter from the surrounding equipment can make the CBS cone jagged, depending upon the intensity of the speckle pattern on the respective pixel. One may shake the sample holder and grab various frames by the CCD and average all of them, to smoothen out the jaggedness to some extent. However, it is not possible to get rid of the speckle resulting from the fixed apparatus, and one has to live with this discrepancy.

Based on our polarisation discrimination technique, which can pick out extremely weak signals buried in noise, and recalling that the CBS signal is polarisation preserving, we developed yet another technique of improving the signal-to-noise ratio in coherent backscattering.

The essence of our method was as follows. Before the backscattered light fell onto the CCD camera, a polariser was inserted in its path. This polariser was mounted on a stepper-motor, and could be rotated about the direction of backscatter. The polariser was rotated in steps of 10°, and at each position of the polariser, a frame was grabbed by the CCD. The CBS curve at six successive positions of the polariser is shown in the figure 4.7.

The gradual degradation in the curves is quite obvious, and so is the jaggedness of the peaks, resulting from the speckle pattern from the surrounding equipment. After grabbing a sufficient number of frames, a time series was built for each pixel. Fourier transforming the time series for each pixel, two images were reconstructed, one was the image at zero frequency, and the other at twice the frequency of rotation of the polariser, say 2ω, similar to the procedure described in imaging using polarisation discrimination.

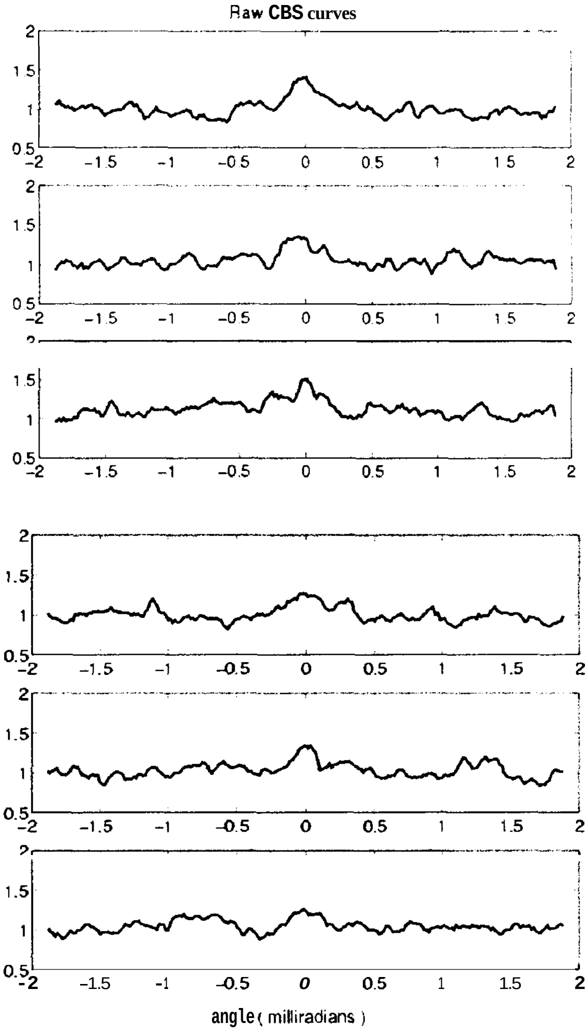

Figure 4.7: *The* CBS *curves obtained at six different positions of the rotating polariser. The jagged profile is due to the stationary speckle pattern, while the variation in the peak intensity is obvious from the series of the curves.*

The image at the zero frequency was the total intensity falling onto the CCD, and equivalent to the image obtained by summing various frames, which is equivalent to averaging them. The image at the frequency 2ω consisted of the polarised content of the backscattered light, i.e., the CBS signal, and the noisy scatter from the surrounding equipment. The CBS plot obtained from the zero frequency image is shown in the figure 4.8, and one can see the enhancement to be just around 1.2.

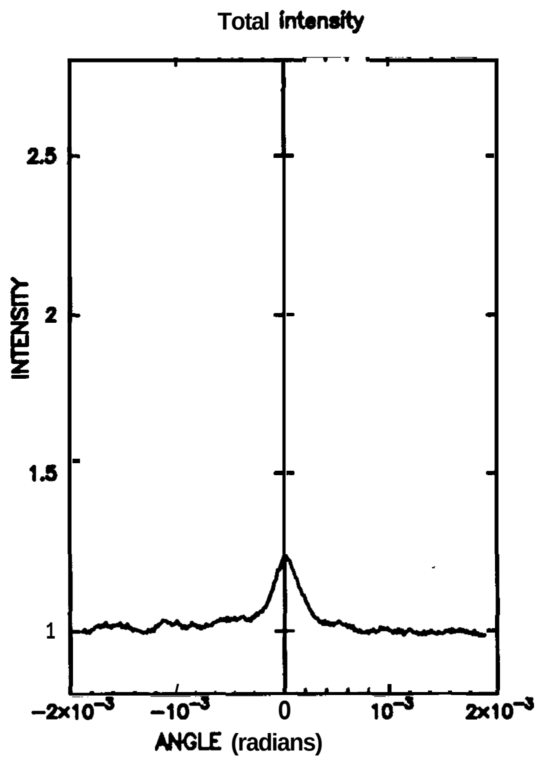

Figure 4.8: *The CBS curve from a sample of* $l^* = 590\mu$. *The signal is too weak, giving an enhancement of* **1.2.** *Comparison of earlier curves shows the weakening of the enhancement and narrowing of the curve upon increasing the* l^*. *A least squares fit does not work on such CBS curves.*

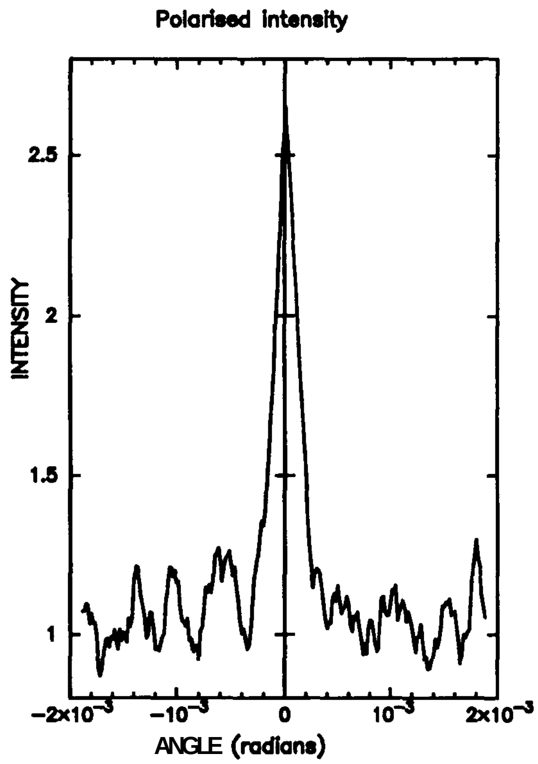

Figure 4.9: CBS *cone obtained using polarisation discrimination. The peak stands out prominently from the noise. The jagged noise here is due to the speckle resulting from reflections from surrounding apparatus. A least squares fit cannot be done to this curve because of the absence of the incoherent noise from the scattering medium.*

The averaging of the speckle is evident from the fact that the CBS curve looks smoothened as compared to the raw data, shown in figure 4.7. The plot from the image at frequency 2ω, as illustrated by figure 4.9, shows the strong signal on the background of the noisy scatter.

The CBS signal is much stronger as compared to the noisy scatter, and the peak stands out marked in its background. The advantage of this method is that, one can gather more frames to construct a longer time series to improve the signal contrast over the background.

However, it should be mentioned that this method separates the coherent backscattered signal from the incoherent noise because of the random polarisation of the noise.

The **1** : **2** enhancement factor assumes the existence of incoherent noise. If this is eliminated, the enhancement factors can exceed **2,** as in the case seen in figure **4.9.** Nonetheless. the method is quite useful in demarcating the signal from the noise, as is obvious from the figure 4.9. If one were to use this technique to characterise coherent backscattering, equations **4.11** and **4.12** have to be suitably modified, and the curves obtained by polarisatiori discrimination suitably normalised. Analysis is underway to recast the polarisation filtered CBS curve in the regular format, to make the process of polarisation discrimination even more useful.

Bibliography

[1] M. P. van Albada and A. Lagendijk, Phys. Rev. Lett. 55, 2692 (1985).

[2] P. Wolf and G. Maret, Phys. Rev. Lett. 55, 2696 (1985).

[3] P. Sheng, *Introduction to Wave Scattering, Localisation and Mesoscopic Phenomena* (Academic Press, San Diego, 1995).

[4] *Scattering and Localisation of Classical waves in random media* in *World Scientific Series on Directions in Condensed Matter Physics 8*, Ed. Ping Sheng (World Scientific, Singapore, 1990).

[5] M. B. van der Mark, M.P. van Albada and Ad Lagendijk, Phys. Rev. B 37, 3575 (1988).

[6] E. Akkermans, P. Wolf, R. Maynard and G. Maret, J. Phys. France 49, 77 (1988).

[7] P. Wolf, G. Maret, E. Akkermans and R.Maynard, J. Phys. France 49, 63 (1988).

[8] G. Mie, Ann. Physik 25, 337 (1908).

[9] H. C. van de Hulst, *Light Scattering by Small Particles*, (Dover, New York, 1981).

[10] *Numerical Recipes in Fortran, The Art of Scientific Computing, W*. H. Press, S. A. Teukolsky, W. T. Vellerling and B. P. Flannery, (Cambridge University Press, 1992).

[11] D. S. Wiersma, P. Bartolini, A. Lagendijk and R. Righini , Nature 390, 671 (1997).